Supplement of Atmos. Meas. Tech., 13, 3799–3813, 2020
https://doi.org/10.5194/amt-13-3799-2020-supplement

Atmospheric Measurement Techniques
Open Access
EGU

Supplement of

A new optical-based technique for real-time measurements of mineral dust concentration in PM_{10} using a virtual impactor

Luka Drinovec et al.

Correspondence to: Luka Drinovec (luka.drinovec@ijs.si)

S1. Virtual Impactor Characterization

The performance of the virtual impactor (VI) was characterized using NIST polystyrene-latex (PSL) spheres with nominal aerodynamic sizes from 0.7 to 10 µm. A schematic of the experimental setup is provided in Figure S1. In brief, particles produced by atomization were consequently dried and their number distribution was measured using an Aerodynamic Particle Counter (APS; TSI mod 3321). The APS was operated with 5 (nominal) and with 1.5 (modified) l min^{-1} sampling flows. The VI was respectively operated at 95 (maximum available) and 75 l min^{-1}, providing total-to-minor flow ratios of 19 (i.e., 95:5) and 50 (i.e., 75:1.5). Since the atomizer used was not capable of providing the above-mentioned total flows, a "Y" junction with a HEPA filter was used downstream the silica diffusion drier for supplementing air into the system (i.e., dilution). For maintaining the total flow and thus the dilution and the particle losses in the system constant, the high flow of the VI was always operational. The concentration of particles was measured before and after the VI using another "Y" junction. For measurements of the particle concentration with the VI, the APS was connected in the minor flow outlet of the VI, while a closed valve was used to block the other outlet of the second "Y" junction (Figure S1 a). Particle concentration before the impactor was measured by connecting the APS directly to the Y junction (i.e., upstream the VI), while the closed valve was put to the low flow outlet of the VI (Figure S1 b). Note that, in the latter case the high flow of the VI was operational as well for maintaining the total flow of the system constant.

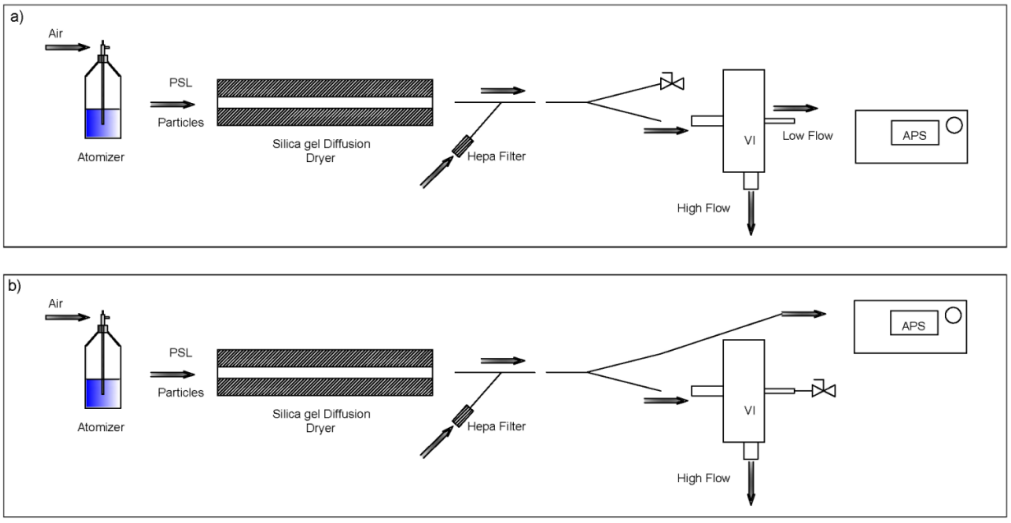

Figure S1. Schematics of the experimental setup for characterizing the performance of the virtual impactor. Particle size distributions were measured using an APS downstream (a) and upstream the VI (b). In both cases the high flow of the VI was operational for maintaining the total flow and consequently the dilution and particle losses in the system constant.

Five samples were collected in each case (i.e., size distribution measured downstream and upstream the VI) for each PSL size and for each set of flow rates. The average measured size distributions were used for calculating the concentration enhancement factor *CE* of the VI at the specific aerodynamic diameters (D), corresponding to the aerodynamic diameters of PSL particles used in each experiment as follows:

$$CE(D) = \frac{C_{VI}}{C} \quad . \tag{S1}$$

The fraction of theoretical concentration efficiency *fCE*, defined as the ratio of the concentration efficiency calculated for each aerodynamic diameter *D*, with the virtual impactor flow ratio *FR* (maximum efficiency) was also calculated as follows:

$$FR = \frac{F_{in}}{F_{out}} \quad , \tag{S2}$$

$$fCE(D) = \frac{CE(D)}{FR} \quad . \tag{S3}$$

Figure S2 shows the results in terms of the enhancement factor for particles having nominal diameter from 0.7 to 10 µm when the VI was operated at two different flow settings, namely 95:5 and 75:1.5 l min^{-1} (i.e., total:minor flow), respectively. Note that, the enhancement factor of 0.5 µm was calculated from the size distributions obtained from measuring particles with nominal diameter of 0.7 µm and that for the flow settings of 75:1.5 l min^{-1} the maximum size of particles measured was 5 µm.

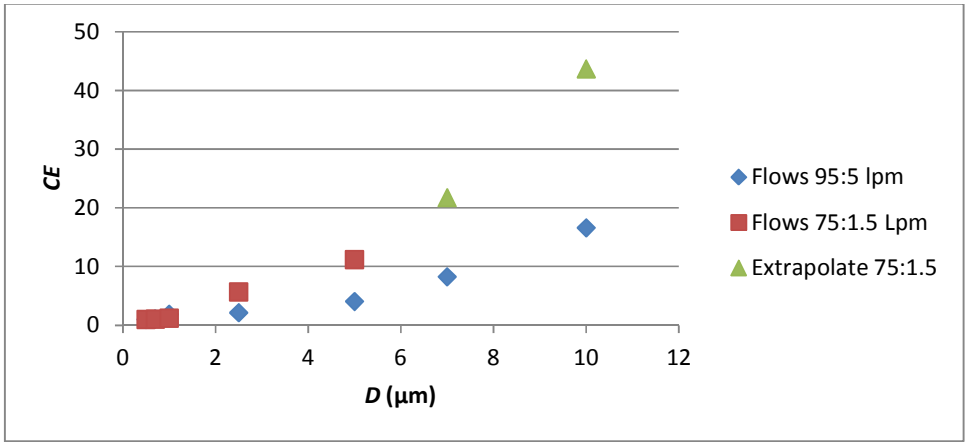

Figure S2. Concentration efficiency for particles having aerodynamic diameters ranging from 0.7 to 10 µm when the VI was operated with 95:5 and 75:1.5 l/min, total:minor flow, respectively. For the larger flow, the concentration efficiency of the larger particles (i.e., 7, 10 µm) is not measured but extrapolated due to poor counting statistics.

Figure S3 shows the results in terms of the fraction of theoretical concentration efficiency (*fCE*) for the measured particles when the VI was operated at two different flow settings. While the measured concentration efficiency is different at each measured size and for each set of flows, the calculated *fCE* is almost identical for each size. This suggests that the enhancement factor of the VI for particle sizes above 1 µm can be estimated if the flow ratio is known. Table S1 shows aggregate results of the experiments conducted and used for producing Figures S1 and S2.

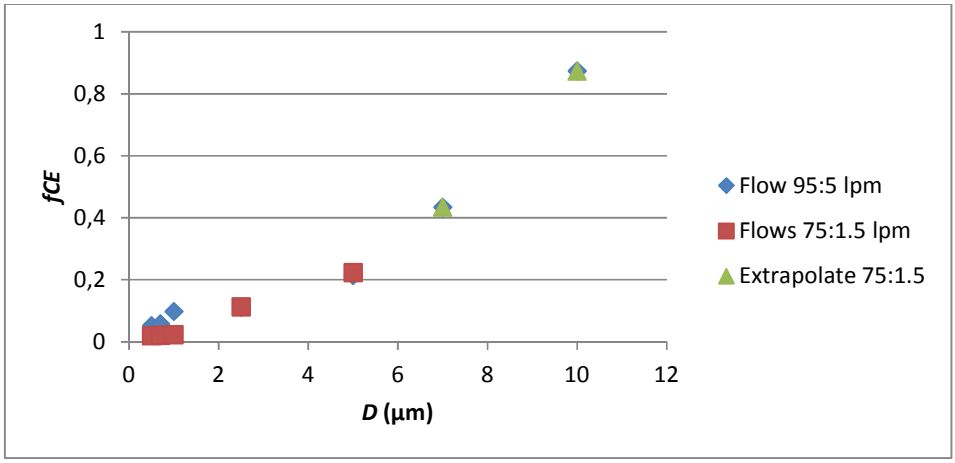

Figure S3. Fraction of the theoretical concentration efficiency (*fCE*) for particles having aerodynamic diameters ranging from 0.7 to 10 µm when the VI was operated with flow ratios 95:5 and 75:1.5, respectively. For the larger flow, the concentration efficiency of the larger particles (i.e., 7, 10 µm) is not measured but extrapolated due to poor counting statistics.

Table S1. Aggregate results of the concentration efficiency (*CE*) and fraction of the theoretical concentration efficiency (*fCE*) of particles having aerodynamic diameters ranging from 0.7 to 10 µm, when the VI was operated with 95:5 and with 75:1.5 flow ratios. Green values are extrapolated.

	Experiment 1 (F_{in}=75 l min^{-1}, F_{out}=1.5 l min^{-1}, *FR*=50)		Experiment 2 (F_{in}=95 l min^{-1}, F_{out}=5 l min^{-1}, *FR*=19)	
***D* (µm)**	***CE***	***fCE***	***CE***	***fCE***
0.5	1.00	0.0200	1.00	0.0526
0.7	1.06	0.0212	1.11	0.0584
1	1.20	0.0240	1.87	0.0984
2.5	5.68	0.1135	2.14	0.1126
5	11.19	0.2238	4.07	0.2142
7	21.74	0.4347	8.26	0.4347
10	43.68	0.8737	16.60	0.8737

S2. Filter loading effect compensation on AE33 with virtual impactor

The automatic compensation of the AE33 failed for the VI measurements and produced faulty values of the compensation parameter k due to the quantum nature of big particles: particles are directed either to spot 1 or spot 2 in the optical chamber of the instrument. Because of the size of these particles, they induce a large signal on one measurement spots at the time (Figure S4), which hinders automatic compensation algorithm (Drinovec et al., 2015) – see variation of parameter k values during the campaign (Figure S5a).

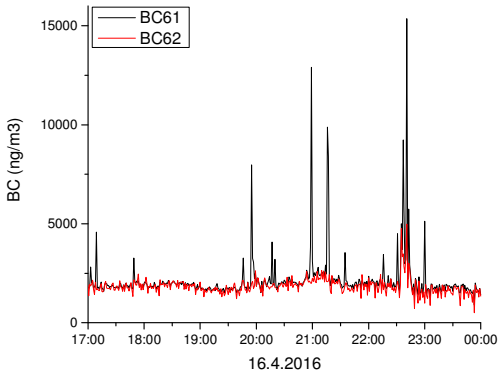

Figure S4. Signal from AE33 connected to the virtual impactor for spot 1 and spot 2.

The loading effect was characterized using the *BC* vs. *ATN* method (Park et al., 2010; Drinovec et al., 2015) using the data between 16 April 2016 and 30 April 2016. The obtained slopes (Figure S2) are used for offline compensation using equation *cBC=BC*/(1-*k***ATN*). The compensated data is again tested using the *BC* vs. *ATN* method (Figure S6).

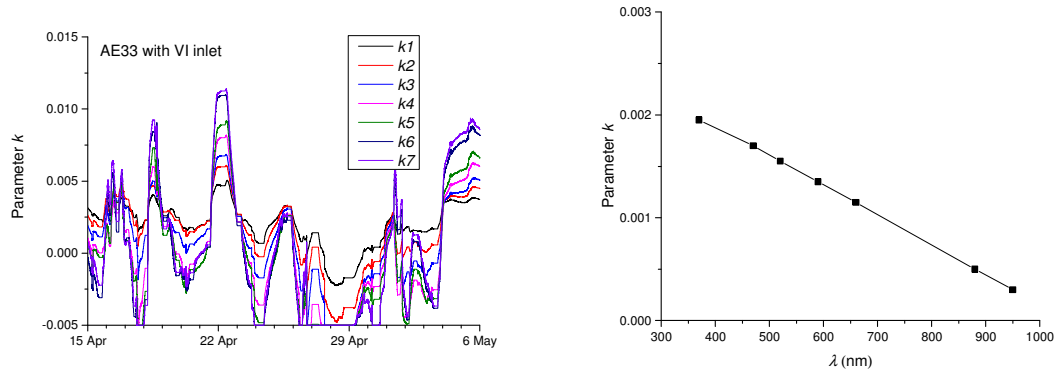

a) b)

Figure S5. The compensation parameter *k* values determined by AE33 (a) and those used for offline compensation of data from Aethalometer with a virtual impactor inlet (b).

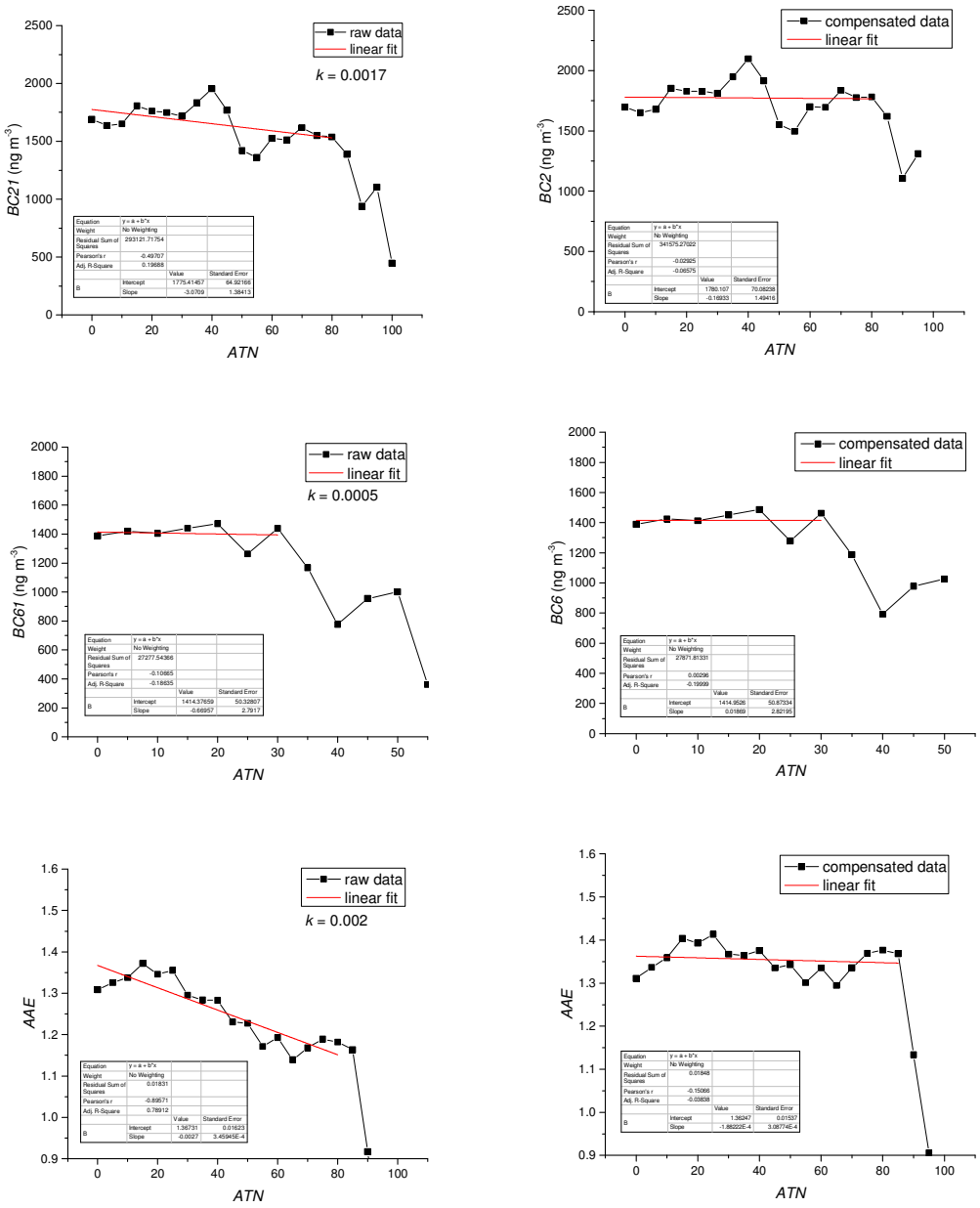

Figure S6. *BC* vs. *ATN* analysis for raw data (left side) and data compensated using fixed k values, derived from the left plot (right side).

S3. Uncertainty of AE33 measurements

The uncertainty of AE33 measurements was determined calculating the ratio of *BC* between instrument with TSP and PM_1 inlets. Because there is almost no dependence of BC_{TSP}/BC_{PM1} ratio on mineral dust concentration (Figure S7), the variation of this parameter results from the measurement uncertainty. Uncertainty of *BC* during the Cyprus campaign is thus calculated as a standard deviation of BC_{TSP}/BC_{PM1} ratio (Table S2).

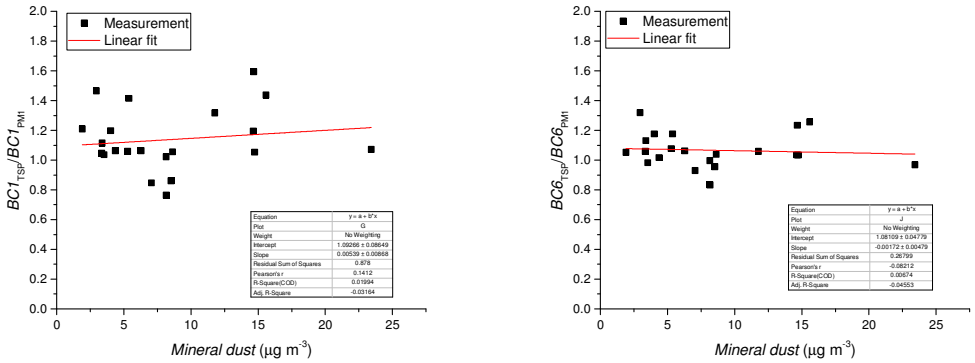

a) b)

Figure S7. Correlation between 24h average ratios BC_{TSP}/BC_{PM1} and Mineral dust concentration for Aethalometer channel 1 (a) and channel 6 (b).

Table S2. Uncertainty estimation during the Cyprus campaign

Wavelength	BC_{TSP}/BC_{PM1}	**Uncertainty for *BC***
370 nm	1.14 ± 0.21	18%
880 nm	1.07 ± 0.12	11%

S4. Correlation between *PM* measurements by TEOM and filter weighting

TEOM and filter measurements data obtained between 15 April 2016 and 6 May 2016 are compared (Figure S8, Table S3). The two methods show high R^2 value and a slope which differs from unity by less than 10%. On average TEOM overestimates *PM* by 2% for $PM_{2.5}$ and 8% for PM_{10}.

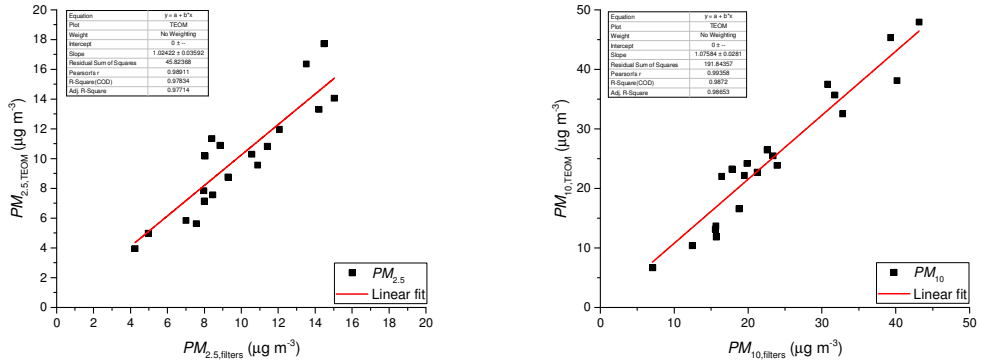

a) b)

Figure S8. Correlation between $PM_{2.5}$ (a) and PM_{10} (b) measured by TEOM and filter weighting.

Table S3. Fitting results for correlation between TEOM and filter weighting method.

	Slope	***R^2***
$PM_{2.5}$	1.02 ± 0.04	0.978
PM_{10}	1.08 ± 0.03	0.987

S5. Correlation between APS and TEOM

The aerodynamic particle size distribution from APS was used to calculate particle volume for PM_{10} and $PM_{2.5}$ size fraction assuming the sphericity of the particles. Particle volume was compared with the particle mass concentrations $PM_{2.5}$ and PM_{10} obtained by TEOM (Figure S9). The correlation is better for sub 10 µm size fraction with R^2 of 0.97. The sub 2.5 µm fraction has a 33% smaller volume/mass slope compared to the sub 10 µm fraction.

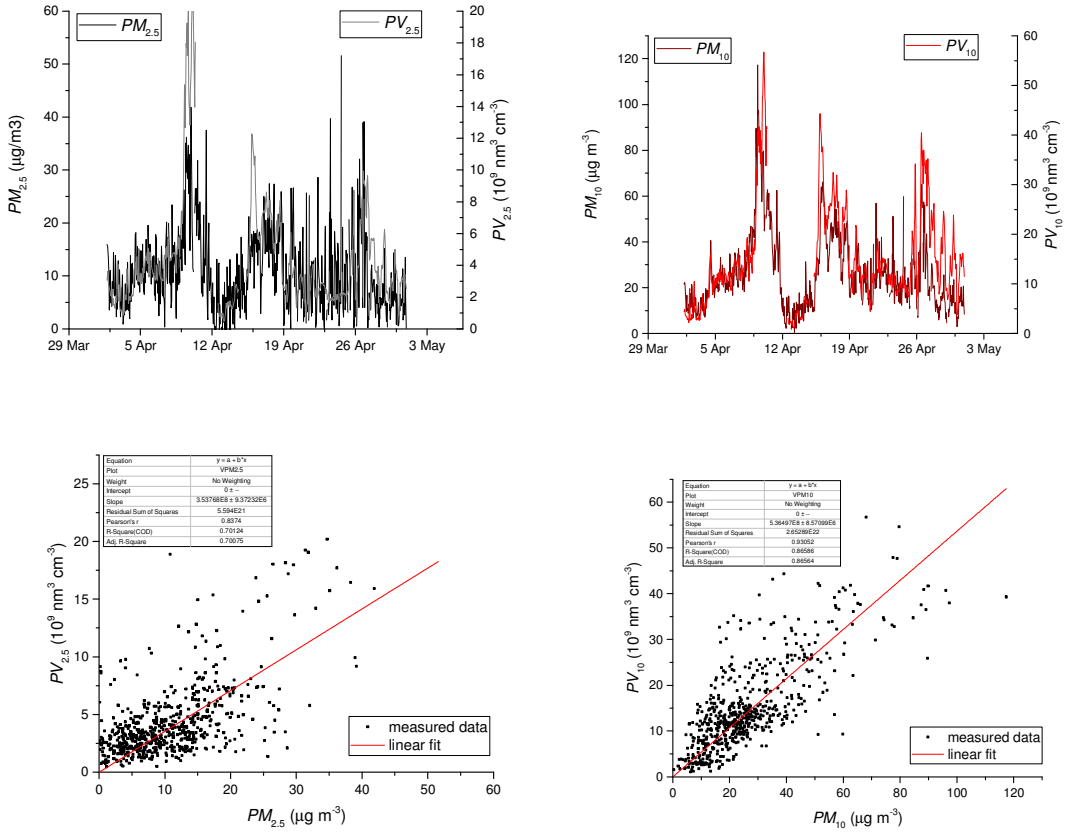

Figure S9. Time series of particle mass concentration (*PM*) and particle volume concentration (*PV*) concentrations in 2.5 µm and 10 µm size fractions (a,b) and correlations (c,d).

Table S4 . Fitting results for correlation between APS and TEOM.

Correlation	*Slope* (µm^{-3} µg^{-1})	R^2
PV_{10} vs. PM_{10}	5.36E5 ± 9E3	0.87
$PV_{2.5}$ vs. $PM_{2.5}$	3.54E5 ± 9E3	0.70

S6. Mass closure on daily PM10 samples

Mass closure was performed by combining PM_{10} from the high volume sampler filters, chemical analysis for cations ($NH4^+$, K^+) and anions (NO_3^-, SO_4^{2-}). Calcium concentration was used to establish mineral dust concentration assuming its 12% mass fraction in mineral dust. Organic matter was calculated from organic carbon concentration (OC) using a organic mass-to-organic carbon factor of 2.

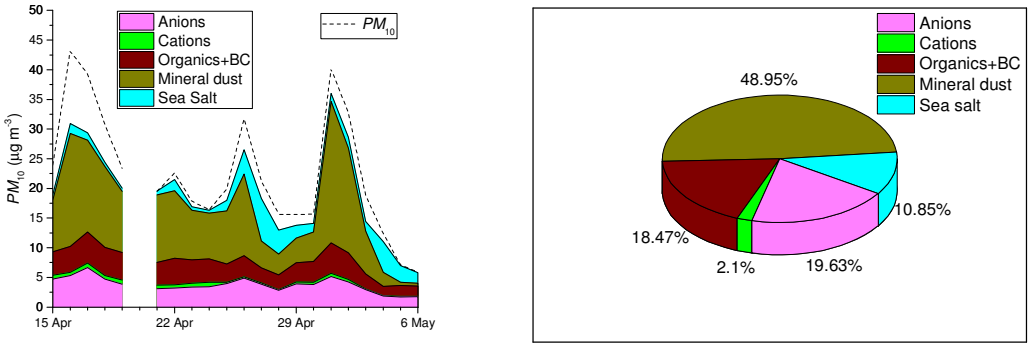

a) b)

Figure S10. Time series (a) and average (b) contributions of different components to PM_{10} (a) during the measurement campaign.

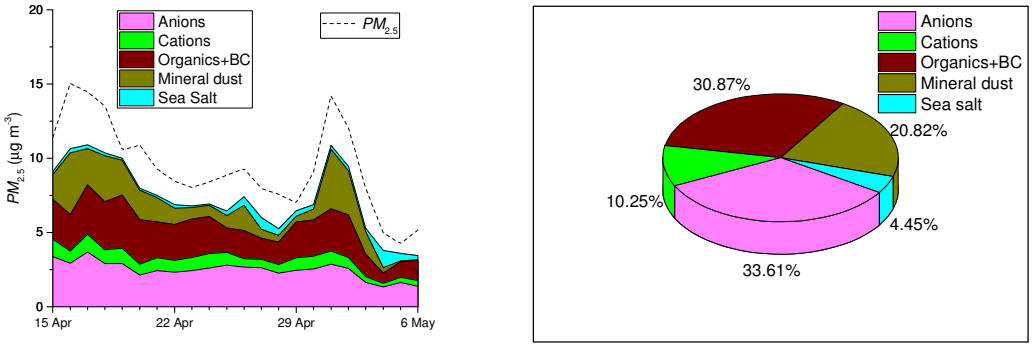

a) b)

Figure S11. Time series (a) and average (b) contributions of different components to $PM_{2.5}$ (a) during the measurement campaign.

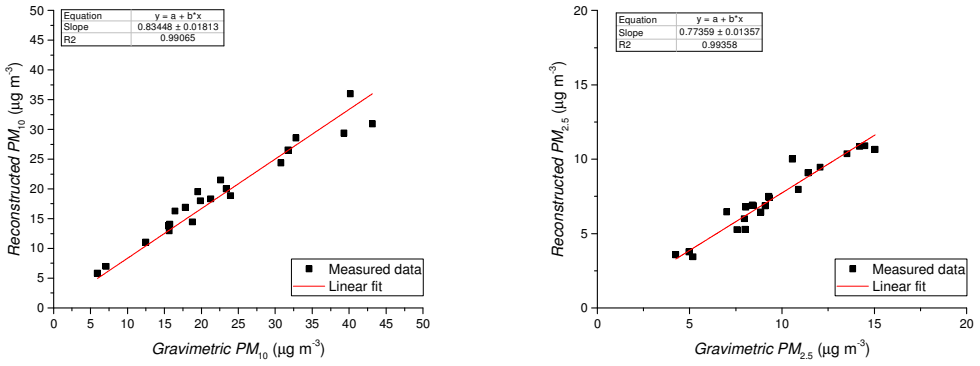

a) b)

Figure S12. Correlation between gravimetric measurements of *PM* and that reconstructed from chemical analysis.

S7. Trace element analysis on PM_{10} filters using inductively coupled plasma mass spectrometry (ICP-MS)

24h PM_{10} filters were analysed for trace elements As, Cd, Pb, Ni, Cr, Fe, Cu, Al, V, Mn, Zn and Ti. *Al* and *Fe* can be used to identify mineral dust (Guieu et al., 2002), showing good correlation with *Ca* obtained by ion chromatography (Figure S13). for the whole year 2016 we obtained average slope between *Al* and *Ca* of 0.58 ± 0.01 and average slope between *Fe* and *Ca* of 0.44 ± 0.01 (Figure S14).

Statistical analysis of chemical ratio *Fe*/*Ca* can give us information on the variability of chemical composition of mineral dust (Table S5) and directly influences the accuracy of the VI-PM1 method.

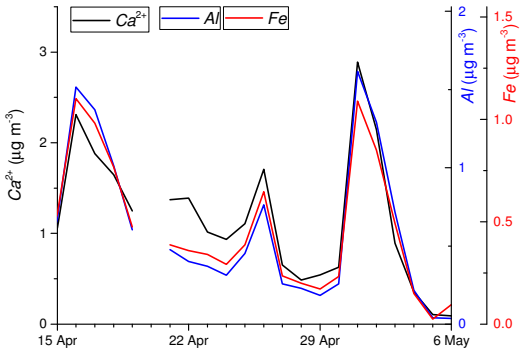

Figure S13. Time series of ambient Ca^{2+}, *Al* and *Fe* concentration in PM_{10} fraction during the calibration campaign

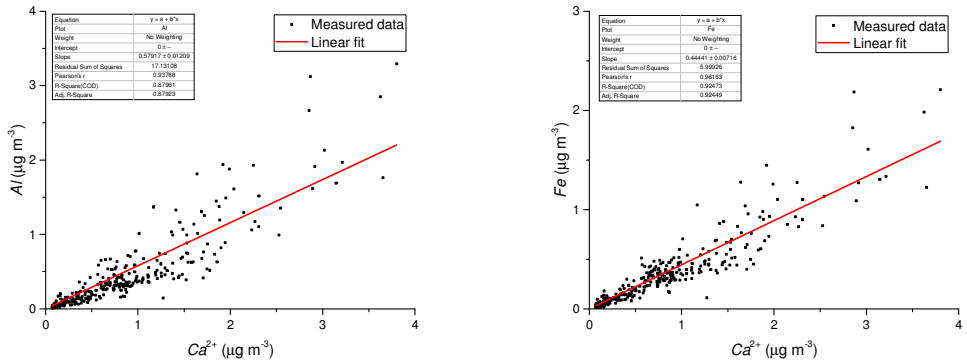

Figure S14. Correlation between *Al* (a) and *Fe* (b) with *Ca* measured on 24h PM_{10} filters. The figures contain data for the whole year 2016.

Table S5. Elemental composition and ratios for iron, calcium and aluminium for the whole 2016 and for the calibration part of the Cyprus campaign.

	Year 2016	Variability	Interval 16.4.2016 – 6.5.2016	Variability
Fe/PM_{10}	0.015 ± 0.008	53%	0.019 ± 0.006	32%
Ca/PM_{10}	0.037 ± 0.017	46%	0.047 ± 0.016	34%
Fe/*Ca*	0.41 ± 0.15	38%	0.42 ± 0.17	40%

S8. Characterization of mineral dust using scanning electron microscopy – energy dispersive X-ray (SEM-EDX) analysis of PM_{10} filters

Several filter samples were analyzed for their elemental composition using energy-dispersive X-ray spectroscopy – similarly to Engelbrecht et al. (2016). An example of SEM-EDX measurement is presented on Figure S15. Each of the selected filter samples was characterized by an average of 10-20 SEM-EDX analyses (Figure S16). The main constituent elements of mineral dust in all filters are oxygen, silica and aluminium. There is a big particle-to-particle variation in the elemental composition. With a higher number of collected particles the uncertainty of the elemental composition is reduced.

The sample from 10 April 2016 contains sodium and chlorine indicating the influence of sea salt. Calcium (0-10%), iron (0-5%) and potassium (0.5-2%) contributions differ a lot between the different filters. Formenti et al. (2008) showed a similar variability of mineral composition for dust from different source regions.

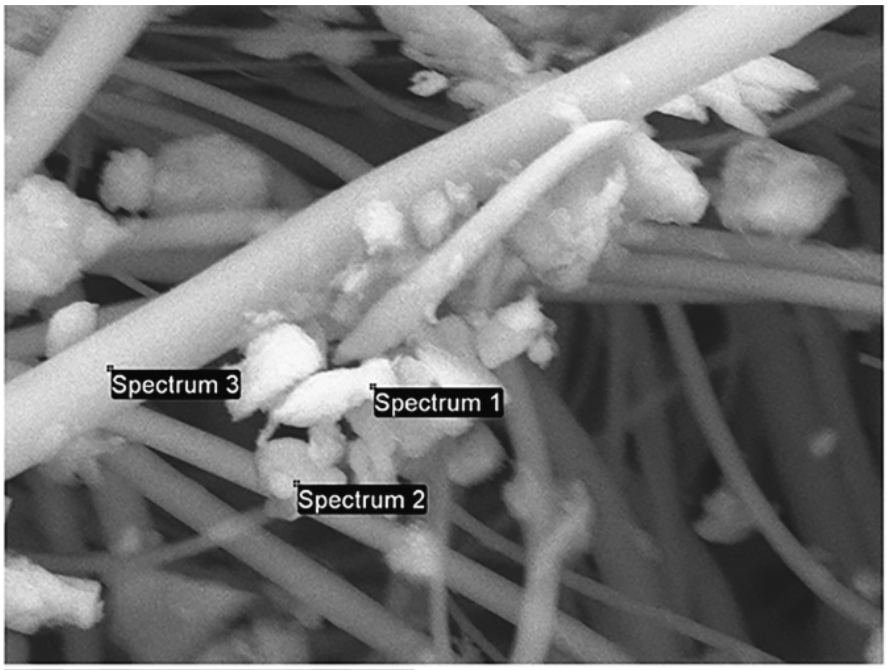

Spectrum	O	Mg	Al	Si	Cl	K	Ca	Fe	Total
Spectrum 1	53.71	0.90	5.52	32.71	0.79	0.79	2.70	2.88	100.00
Spectrum 2	57.97	0.85	5.57	29.72	0.61	0.80	1.72	2.77	100.00
Spectrum 3	63.86			36.14					100.00

All results in weight%

Figure S15. SEM-EDX analysis of particles (Spectrum 1 & 2) collected on the quartz fiber filter (Spectrum 3).

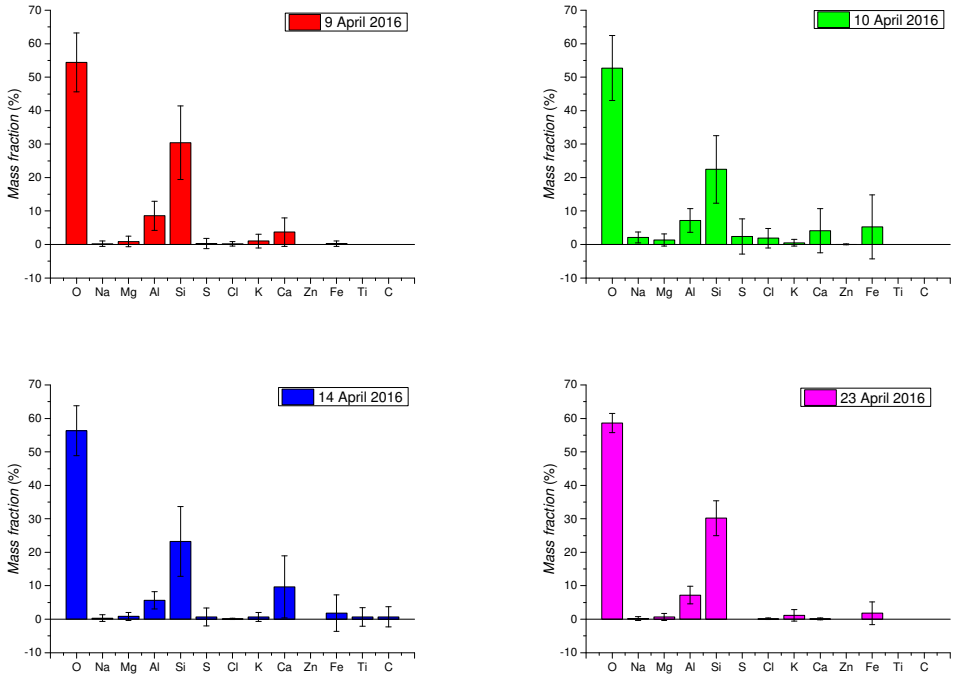

Figure S16. Elemental composition of mineral dust filter samples obtained using EDX spectroscopy. The error bars show the standard deviation of 10-20 measurements on each sample.

References

Drinovec, L., Močnik, G., Zotter, P., Prévôt, A. S. H., Ruckstuhl, C., Coz, E., Rupakheti, M., Sciare, J., Müller, T., Wiedensohler, A., and Hansen, A. D. A.: The "dual-spot" Aethalometer: an improved measurement of aerosol black carbon with real-time loading compensation, Atmos. Meas. Tech., 8, 1965-1979, https://doi.org/10.5194/amt-8-1965-2015, 2015.

Engelbrecht, J. P., Moosmüller, H., Pincock, S., Jayanty, R. K. M., Lersch, T., and Casuccio, G.: Technical note: Mineralogical, chemical, morphological, and optical interrelationships of mineral dust re-suspensions, Atmos. Chem. Phys., 16, 10809-10830, https://doi.org/10.5194/acp-16-10809-2016, 2016.

Formenti, P., Rajot, J. L., Desboeufs, K., Caquineau, S., Chevaillier, S., Nava, S., Gaudichet, A., Journet, E., Triquet, S., Alfaro, S., Chiari, M., Haywood, J., Coe, H. and Highwood, E.: Regional variability of the composition of mineral dust from western Africa: Results from the AMMA SOP0/DABEX and DODO field campaigns, J. Geophys. Res., 113, D00C13, doi:10.1029/2008JD009903, 2008.

Guieu, C., Lo¨ye-Pilot, M.-D., Ridame, C., and Thomas, C.: Chemical Characterization of the Saharan dust end-member: Some biogeochemical implications for the Western Mediterranean sea, J. Geophys. Res., 107, doi:10.1029/2001JD000582, 2002.

Park, S. S., Hansen, A. D. A., and Cho, Y.: Measurement of real time black carbon for investigating spot loading effects of Aethalometer data, Atmos. Environ., 11, 1449–1455, doi:10.1016/j.atmosenv.2010.01.025, 2010.